DOI: 10.1557/adv.2019.67

The Role of Nano-crystallites on Conduction Mechanisms of Current Through Ag Gridlines of Si Solar Cells

Keming Ren, Tang Ye, Yong Zhang and Abasifreke Ebong

University of North Carolina at Charlotte, 9201 University City Blvd, Charlotte, NC 28223, U.S.A

ABSTRACT

In order to understand the impact of nano-crystallites on current transport mechanisms in screen-printed c-Si solar cells with lowly-doped emitter, Te-glass based Ag pastes with different transition temperatures (T_g) were used. The Te-glass with lower T_g showed lower R_c than the one with higher T_g due to the formation of nano-crystallites in the glass layer. These nano-crystallites enhance the conductivity of the glass and lead to higher fill factor (FF). The nature of these nano-crystallites was first identified by the Raman spectrometry and the peaks at 76 cm^{-1}, 119 cm^{-1} and 145 cm^{-1} were corresponding to Ag_2Te and PbTe. The conductive-AFM further confirmed the high conductivity of these nano-crystallites without pyramidal Ag crystallites, which means the current transporting from Si emitter to Ag gridlines is mainly through the nano-crystallites in the glass.

INTRODUCTION

For solar electricity to reach \$0.03 kW/h in 2030 as predicted by the Department of Energy (DOE) [1], the efficiency of solar cells must approach the material limit. For instance, Si which holds the largest market share in solar industries, its theoretical efficiency can be ~30% [2]. However, since the efficiency is a product of the open circuit voltage (V_{OC}), short circuit current density (J_{SC}) and *FF*, these parameters must be increased simultaneously. In a study by ITRPV [3], the lowly-doped emitter with sheet resistance ~140 Ω/sq is the target to achieve high efficiency by enhancing both V_{OC} and J_{SC}, because the lowly-doped emitter is more transparent to photons. But it is hard to contact such emitter with high *FF* >82% and it requires a new understanding of the screen-printed contacts on the lowly-doped emitter (~140 Ω/sq).

To achieve high *FF*, the total series resistance (R_s) encompassing emitter, gridline, busbar, bulk, back and contact (Si/Ag-gridline) should be very low. Technically, the emitter resistance is addressed by decreasing the finger spacing; gridline resistance is reduced by improving the paste rheology to fabricate continuous and thick gridlines plus increasing the number of busbars; busbar resistance is decreased by increasing the weight percent (wt.%) of Ag solids in the paste and avoiding line breakage; bulk resistance is fixed and the resistivity normally is ~2 Ω-cm to reduce the light; back resistance is lowered by having uniform Al alloying in the ~10% back contact area and for the aluminium back surface field (Al-BSF) solar cells, uniform BSF is important. This leaves the front contact resistance (Si/Ag-gridline), which is said to depend on the emitter peak surface concentration. The highest *FF* reported today on screen-printed solar cells, for example, Al-BSF cell is 80.92% [4] and that of the passivated emitter and rear cell (PERC) is 81.49% [5]. In this work, the role of nano-crystallites formed in the glass on current conduction between Si and gridlines is assessed. The formation of such nano-crystallites in the glass is seen to reduce the contact resistance and lead to high *FF*.

THEORY

Contact resistance and current transport mechanisms at the Si/Ag-gridline contacts

According to Goetzberger [6], contact resistance (R_c) is given as

$$R_c = \frac{\rho_c}{l \times L} \qquad (1)$$

where l is the length and L is the width of the gridline and ρ_c is specific contact resistance given by [7]

$$\rho_c = \frac{k}{qTA^*} . \exp\left(\frac{4\pi\sqrt{\varepsilon_{Si} m^*}}{h} . \frac{\Phi_{Bn}}{\sqrt{N_s}}\right) \qquad (2)$$

where k is the Boltzmann constant, q is the elementary charge, T is the temperature in K, A^* is the effective Richardson constant, ε_{Si} is the permittivity of Si, m^* is the effective mass of the charge carriers, h is the Planck constant, Φ_{Bn} is the metal-semiconductor barrier height and N_s is the surface doping concentration.

From equation (1), the geometry (l and L) of the gridline has an impact on R_c and could be optimized by changing the number of busbars (BB) [8] and narrowing the gridline separation [9]. Eventually, R_c is dependent on ρ_c. According to equation (2), lowly-doped emitter has higher ρ_c due to low N_s and hence higher R_c. In addition, for the screen-printed technology, the Ag gridlines are contacting not right on the top of Si surface, but several nanometers underneath it. It was found that the concentration of phosphorus decreased dramatically as the depth and it showed from the top surface to below 33 nm, the N_s decreased from $5\text{x}10^{20}$ cm^{-3} to $1\text{x}10^{20}\text{cm}^{-3}$ [10]. Moreover, the contact between Ag gridlines and Si emitter is not pure metal-semiconductor contact. It has a thin glass layer and metal crystallites at the interface [11]. The effect of the thin glass layer and the Ag crystallites on the current transport mechanisms is unclear. One well-accepted hypothesis is that the major current flow into the Ag gridlines is through the pyramidal Ag crystallites which directly contact with bulk Ag. This hypothesis was supported by conductive-AFM [12], microscopic I-V measurement [13] and theoretically calculation [14]. However, some researchers found that the pyramidal Ag crystallites were not necessary for a low R_c and high efficiency was achieved without pyramidal Ag crystallites [15]. In addition, the electron tunnelling assisted by nano-Ag colloids in the interface glass played a more important role in current transport mechanisms than the Ag crystallites. The more Ag colloids in the glass layer, the lower the R_c [16].

To understand the current transport mechanisms in the solar cell front contacts and reduce R_c, one main method is to modify the Ag paste constituents, which contain metal powder (~85%), glass frits (~5%), organic binder (~10%) and additives such as phosphorus dopant (PV168), Al, Cu etc. The addition of phosphorus dopant [17] did not yield any useful results because of the longer time it required for the phosphorus doping to the contact region, the higher firing temperature ($\geq 835\ ^{o}C$) and forming gas annealing [18]. In addition, the Al additives needed to be fired under optimized temperature to avoid forming Al-Si alloy and shunting the p-n junction [19]. Furthermore, the Cu additive led to the formation of CuO_x during the firing and requires forming gas annealing[20].

The alternative way to modify paste is using the glass frits with different transition temperatures (T_g) and crystallization behaviours [11, 21]. By changing the ratio of TeO_2/ZnO [22], TeO_2/PbO [23, 24], and TeO_2/Bi_2O_3 [25], the T_g of glass frits were changed. It was found that during the contact formation process, the glass frits with too low T_g started to flow earlier during the firing. There were two results: (1) the glass frits had earlier fluidization to etch the anti-reflection coating (ARC) and an earlier dissolution of Ag particles [11]. As a result, large Ag-crystallite precipitates were formed to penetrate the junction. (2) The glass frits would soften and flow more easily to form a thicker glass layer, which prevented photoelectrons from being collected. For high T_g glass frits, they needed higher sintering temperature and had insufficient time to wet the Si surface, which caused an incomplete etching of ARC and had gaps between gridlines and emitter. Thus, the *FF* was low [24]. However, the function of TeO_2 in glass frits is not completely understood and the formation of Ag_2Te and PbTe after contact formation process have not been studied. In this paper, (1) Raman Spectrometer, (2) conductive-AFM, (3) SEM, and (4) EDS analyses have been used to elucidate the formation of Ag_2Te and PbTe, which are believed to decrease the R_c for lowly-doped emitter.

EXPERIMENT

The p-type Czocralski wafers with bulk resistivity of ~2.5 Ω-cm were textured and followed by phosphorus diffusion at $890^{o}C$ to form 95 Ω/sq emitter. After that, the wafer edges were isolated and the phosphorus glass was removed followed by PECVD SiNx (73 nm) deposition. The wafers were divided into four groups for four Ag pastes (A, B, C, D) based on TeO_2 glass with different T_g. Three-busbar structure for full Al-BSF was used in this experiment. The four front Ag pastes were screen-printed in turn onto the wafers with back Al contact already printed and dried. After drying the front Ag paste, the cells were co-fired in the rapid thermal processing (RTP) infrared belt furnace at 230 inch per minute (ipm) at $815^{o}C$ peak temperature. The fabricated cells were first characterized by light I-V measurements, then one cell from each group was cut into 2 mm strip and the contact resistance was measured.

To investigate the contact interface between the underlying Si and gridline, the cut samples were generated into three sets, (a) as fired (AF); (b) Ag metal removed by HNO_3 but the glass remained (HNO_3); and (c) the remained glass removed by *HF* (HF). However, from the contact resistance measurements, the contact resistance for pastes B to D were similar, therefore, other analyses were carried out on samples only with pastes A and D, with highest and lowest R_c and R_s. The microstructure, elemental composition and conductive properties of these samples were evaluated with field-emission scanning electron microscope (FESEM) with EDS (FEI Verios 460L), Raman spectrometer (HORIBA, XploRa^{TM}PLUS) excited at 532 nm and conductive-AFM (Asylum MFP-3D).

RESULTS AND DISCUSSION

Chemical reactions during contact co-firing step

The front Ag contacts are formed by sintering Ag paste under IR belt with temperatures ranging from 400-815°C for a short time. As the temperature increases from low to high, (a) the organic binder burns out; (b) glass frits start to melt and diffuse towards the wafer surface; (c) the melted glass etches away the ARC layer on the wafer surface through the reduction reactions (1) and (2); after ARC removal, the glass starts to react with the Si substrate through reactions (3) [26] and (4) [27]; meanwhile, the formed Pb and Te could further react with Ag and form PbTe and Ag_2Te from reactions (5) and (6).

$$Si_3N_4\,(s) + 6PbO\ (\text{in glass}) \longrightarrow 3SiO_2\,(s) + 6Pb\ (s) + 2N_2\,(g) \quad (1)$$
$$Si_3N_4\,(s) + 3TeO_2\,(\text{in glass}) \longrightarrow 3SiO_2\,(s) + 3Te\ (s) + 2N_2\,(g) \quad (2)$$
$$Si\ (s) + 2PbO\ (\text{in glass}) \longrightarrow SiO_2\,(s) + 2Pb\ (s) \quad (3)$$
$$Si\ (s) + TeO_2\,(\text{in glass}) \longrightarrow SiO_2\,(s) + Te\ (s) \quad (4)$$
$$Pb\ (s) + Te\ (s) \longrightarrow PbTe\ (s) \quad (5)$$
$$2Ag\ (s) + Te\ (s) \longrightarrow Ag_2Te\ (s) \quad (6)$$

Based on Gibbs free energy, the thermodynamic potential for each possible reaction is shown in Figure 1(a) where the potential of reactions (5) and (6) at 850°C is respectively -69.54 kJ/mol and -59.36 kJ/mol. It is obvious that for the reactions (1) ~ (6), the Gibbs free energy is always negative from 300°C to 850°C, which means each reaction can happen spontaneously.

R_c, R_s and *FF of samples with four pastes*

Figure 1b and 1c depict R_c, R_s and the corresponding *FF* for the four pastes. Paste A shows the highest R_c and R_s with lowest *FF*. The high R_c for contacts with paste A can be attributed to the thicker glass layer (~3 μm) in Figure 2a at the interface of Si/Ag-gridline, while the lower R_c for paste D contacts is evident in the thinner glass layer of ~0.7 μm in Figure 2b.

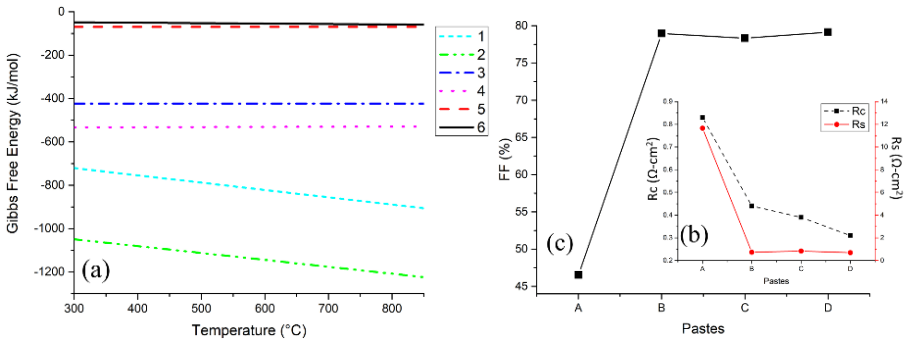

Figure 1, (a) Gibbs free energy for possible reactions (1) ~ (6) under temperature from 300°C to 850°C. (b) R_c and R_s of pastes A-D with (c) *FF*

SEM and EDS analyses

To understand the metal-semiconductor contact interface for the samples with pastes A and D, the microstructure analyse was carried out as shown in Figures 2a and 2b, respectively. The contact with paste A exhibits a thick non-uniform interface glass layer of ~3µm thickness as opposed to those of D with a uniform glass layer of ~0.7 µm and some Ag nano-particles (~50 nm) inside. Figures 2c and 2d, respectively, show the corresponding EDS for the glass frits in pastes A and D along with the Pb:Te ratio of 3.1 and 1.6 respectively. The Pb:Te ratio is known to impact the T_g of the glass [11, 21]. Since the glass frit in paste A had higher T_g than that of D, it is possible that higher firing temperature is needed for the glass frits to melt, wet the Si surface, uniformly etch the SiN_x, and then form a thin glass layer with nano-particles inside as in D.

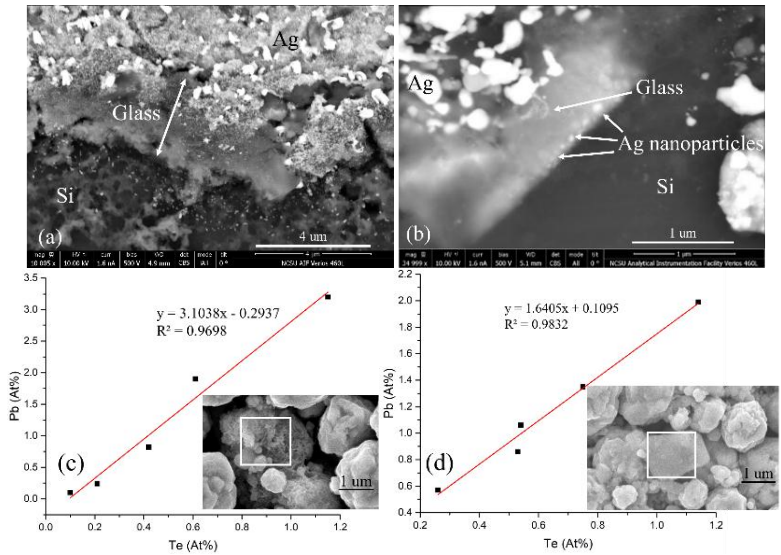

Figure 2, SEM images of samples with pastes (a)A and (b)D with Pb:Te ratio of the glass frits in pastes (c) A and (d) D.

Figure 3a and 3b show the EDS and SEM of the sample with paste A after the Ag gridline was removed with HNO_3. This is an attempt to investigate the location of the nano-particles in the glass, as HNO_3 only removes the Ag gridline without attacking the glass. As seen in Figure 3b, there are only few nano-crystallites and the elemental analysis shows no Te in the analysed region. On the contrary, Figure 3d for paste D, shows micro-sized bright areas which are large nano-crystallites and such nano-crystallites contain Pb, Ag and Te.

In order to further ascertain the location of these large nano-crystallites, the glass layer was etched off with *HF*. Because the sample with paste A did not show any crystallites, EDS was carried out only on paste D after *HF* treatment. As shown in Figure (f), there was few Ag crystallites in the Si for D which indicates the large nano-crystallites were formed right in the glass layer.

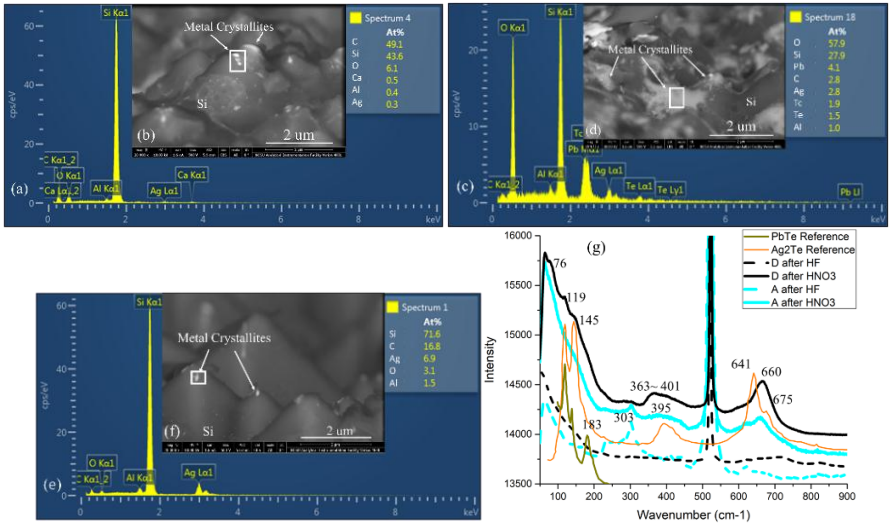

Figure 3, EDS elemental analyses of pastes (a) A, (c)D after HNO_3 treatment and (e) D after *HF*, where the analysed areas are marked by boxes as shown in SEM images: (b) A, (d) D after HNO_3 and (f) D after *HF*. And Raman spectroscopy (g) of pastes A and D after HNO_3 and *HF* treatment.

Raman spectrometer

In order to fully understand the nature of the nano-crystallites formed in the glass layer, the Raman spectroscopy was used. As shown in Figure 3(g), after the HNO_3, D exhibits peaks at 76 cm^{-1}, 119 cm^{-1} and 145 cm^{-1} which match the Ag_2Te and PbTe [28-30]. The peaks around 360-400 cm^{-1} and 660 cm^{-1} are binding vibrations of TeO_2 [31]. For A, it only has TeO_2 peaks and no Ag_2Te and PbTe. After the *HF* treatment, both pastes A and D only show Si peaks at 303 cm^{-1} and 520 cm^{-1}. The Raman spectroscopy confirms that the nano-crystallites formed in the glass for D contains Ag_2Te and PbTe.

Conductive-AFM

In order to understand the distribution of nano-crystallites in the current transport, the glass conductivity was studied by conductive-AFM, where the samples had Ag gridlines removed by HNO_3. The current was measured on the front side after applying a 10V bias on the backside of the sample. In Figure 4d, the sample with paste D has micro-sized areas which is very conductive with current over 10 nA, while most area of sample A is non-conducting. The conductive area in D matches the size and shape of the large nano-crystallites in Figure 3(d). This suggests that the nano-crystallites in the glass layer enhance the glass conductivity and without these nano-crystallites, the glass is insulator. Thus, the current transports from Si emitter to Ag gridlines mainly through these nano-crystallites of Ag_2Te and PbTe.

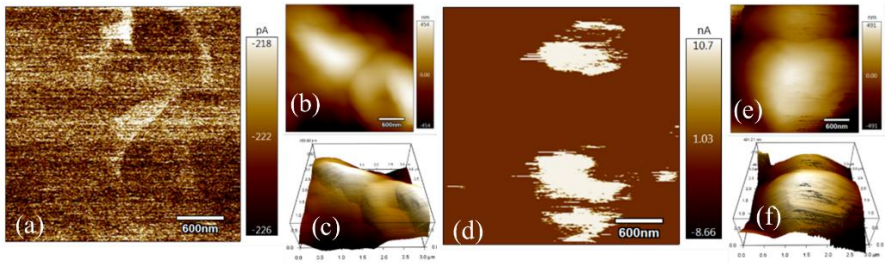

Figure 4, Conductive-AFM measurements on samples with pastes A (a~c) and D (d~f) according to current (a&d), height (b&e) and 3D geometry (c&f) measurement.

CONCLUSIONS

In this study, it is found that the Pb to Te ratio as well as the T_g of the glass frits can impact the reformed glass at interface of Si/Ag-gridline after contact sintering step. The glass with lower T_g enhances the uniform wetting of the Si surface and SiN_x etching as well as the formation of thinner glass layer with large nano-crystallites. These large nano-crystallites embedded in the glass contain Ag_2Te and PbTe and increase the glass conductivity. Thus, the current transport from the Si material to Ag gridline is mainly through these nano-crystallites in the glass. In addition, since the pyramidal Ag crystallites were not found in the emitter after the glass layers removal, it suggests that the interface glass plays a more important role in current transport mechanisms than the Ag crystallites.

REFERENCES

[1] Sunshot 2030. Available at: https://www.energy.gov/eere/solar/sunshot-2030 (accessed 25 November 2018)
[2] W. Shockley and H. J. Queisser, J. Appl. Phys, **32,** 510-519(1961).
[3] ITRPV ninth edition, September 2018. Available at: http://www.itrpv.net/Reports/Downloads/ (accessed 25 November 2018)
[4] K. H. Kim, C. S. Park, J. D. Lee, J. Y. Lim, J. M. Yeon, I. H. Kim, E. J. Lee and Y. H. Cho, Jpn. J. Appl. Phys, **56,** 08MB25(2017,).
[5] W. Deng, F. Ye, R. Liu, Y. Li, H. Chen, Z. Xiong, Y. Yang, Y. Chen, Y. Wang and P. P. Altermatt, 44th IEEE PVSC (2017).
[6] A. Goetzberger, J. Knobloch and B. Voss, Crystalline silicon solar cells. (John Wiley & Sons, 1998) p 105.
[7] C. Ballif, D. Huljić, G. Willeke and A. Hessler-Wyser, Appl. Phys. Lett, **82,** 1878-1880 (2003).
[8] N. Chen and A. Ebong, Sol. Energy Mater Sol. Cells, **146,** 107-113 (2016).
[9] N. Chen, K. Tate and A. Ebong, Jpn. J. Appl. Phys, 2015, **54,** 08KD20(2015).
[10] F. Ye, D. Weiwei, D. Chen, Y. Chen, D. Jianwen, J. Ding, N. Yuan, Z. Feng and P. Verlinden, 2014 EU PVSEC (2014).
[11] M. M. Hilali, S. Sridharan, C. Khadilkar, A. Shaikh, A. Rohatgi and S. Kim, J. Electron. Mater, **35,** 2041-2047 (2006).
[12] G. Grupp, D. Huljic, R. Preu, G. Willeke and J. Luther, Proc. 20th EC PVSEC (2005).
[13] S. Kontermann, G. Willeke and J. Bauer, Appl. Phys. Lett, **97,** 191910 (2010).
[14] S. Kontermann, R. Preu and G. Willeke, Appl. Phys. Lett, **99,** 111905 (2011).
[15] Z. Li, L. Liang and L. Cheng, AIP (2009).
[16] P. Kumar, M. Pfeffer, B. Willsch, O. Eibl, L. J. Koduvelikulathu, V. D. Mihailetchi and R. Kopecek, Sol. Energy Mater Sol. Cells, **157,** 200-208 (2016).
[17] A. Rohatgi, M. M. Hilali, D. Meier, A. Ebong, C. B. Honsberg, A. Carroll and P. Hacke, Georgia Tech (2001).
[18] M. M. Hilali, M. M. Al-Jassim, B. To, H. Moutinho, A. Rohatgi and S. Asher, J. Electrochem. Soc, **152,** G742-G749 (2005).
[19] L. Liang, Z. Li, L. Cheng, N. Takeda and A. Carroll, J. Appl. Phys, **117,** 215102 (2015).

[20] W.-H. Lee, T.-K. Lee and C.-Y. Lo, Journal of Alloys and Compounds, 2016, 686, 339-346.
[21] J. Jiang, Y. He, Z. Zhang, J. Wei and L. Li, J. Alloy. Comp., **689,** 662-668 (2016).
[22] X.-X. Pi, X.-H. Cao, Z.-X. Fu, L. Zhang, P.-D. Han, L.-X. Wang and Q.-T. Zhang, Acta Metallurgica Sinica, **28,** 223-229 (2015).
[23] J. Qin, W. Zhang, S. Bai and Z. Liu, Sol. Energy Mater Sol. Cells, **144,** 256-263 (2016).
[24] G. Zheng, Y. Tai, H. Wang and J. Bai, J. Mater. Sci. Mater. Electron, **25,** 3779-3786 (2014).
[25] F. Ming, C. Si-Guo, W. Yue, Z. Hong and F. Lin, J. Inorg. Mater., **31,** 785-790 (2016).
[26] H. Wang, S. Ma, Q. Ma, X. Cheng, H. Wang and J. Bai, J. Mater. Sci. Mater. Electron, **28,** 6936-6949 (2017).
[27] M. Kurahashi, N. Shindo, K. Nishimura, K. Shirasawa and H. Takato, 7th WCPEC, 1033-1036 (2018).
[28] A. Qin, Y. Fang, P. Tao, J. Zhang and C. Su, Inorg. Chem, **46,** 7403-7409 (2007).
[29] T. Milenov, T. Tenev, I. Miloushev, G. Avdeev, C. Luo and W.-C. Chou, Springer, (2013).
[30] B. Zhang, C. Cai, H. Zhu, F. Wu, Z. Ye, Y. Chen, R. Li, W. Kong and H. Wu, Appl. Phys. Lett, **104,** 161601 (2014).
[31] K. Ren, V. Unsur, A. Chowdhury, Y. Zhang and A. Ebong, 7th WCPEC, 1051-1054 (2018).